Int. J. Heat Mass Transfer. Vol. 27, No. 11, pp. 2119–2131, 1984
Printed in Great Britain

0017-9310/84 $3.00 + 0.00

Coupled radiative and conductive heat transfer across honeycomb panels and through single cells

K. G. T. HOLLANDS,* G. D. RAITHBY,* F. B. RUSSELL† and R. G. WILKINSON‡

*Department of Mechanical Engineering, University of Waterloo, Waterloo, Ontario N2L 3G1, Canada;
†Westinghouse Canada Inc., Hamilton, Canada; ‡Nortec Solar Industries, Manotick, Canada

(*Received* 17 *October* 1983 *and in revised form* 8 *March* 1984)

Abstract—In the absence of natural convection, heat flows through a gas-filled honeycomb by conduction and radiation. For the parameter ranges of interest in a plastic honeycomb inside a flat plate solar collector, the conduction and radiation are strongly coupled. The total heat transfer across the panel was studied experimentally and theoretically. The experimental approach precisely measured the total heat transfer under varying conditions. The theoretical approach proposed several models, established their governing equations, and solved the equations by either numerical or analytical methods. A model based on grey surfaces, specular sidewalls, and one-dimensional conduction yielded results within 6% of measurements.

1. INTRODUCTION

PREDICTING the heat transfer across a honeycomb panel, like the one in a honeycomb solar collector [1], poses a problem in radiative and conductive heat transfer. In the panels of interest (Fig. 1) thin plastic walls compartmentalize the space between two parallel plates, each of which is at a different temperature. A quiescent§ gas fills the compartments (or cells). Whereas the gas is radiantly transparent, the walls are diathermanous, and the plates are opaque. Practical considerations (including the need to keep the gas quiescent) dictate rough values for certain of the parameters: in Fig. 1, w and L are roughly 10 and 50 mm, respectively, and the plate temperatures are about 300 K. For these parameter settings, neither the radiative nor the conductive heat transfer mode dominates, and the two modes are strongly coupled. Thus only a theory amalgamating the two modes can fully resolve the problem.

This paper focuses on the inter-mode coupling and its effect on the total heat transfer. Previous honeycomb analyses [1, 3–5] have ignored the coupling: these decoupled mode analyses (DMA) have assumed that the total heat transfer is the sum of a purely conductive transfer—calculated by ignoring radiation—and a purely radiative transfer—calculated by ignoring conduction.

Most related work has concentrated on the purely-radiative problem, which, because of a certain symmetry, can be reduced to finding the heat transfer through a single cell. The radiative transfer in single cells of various cross-sectional shapes has received extensive study, the work being recently reviewed by Edwards [6]. An early study by Hottel and Keller [7] solved the radiant problem for circular and rectangular cells with diffuse walls and black plates. Specular walls give substantially more heat transfer than diffuse walls—particularly for low wall emissivity; Edwards and Tobin [8] solved the specular (and polarizing) wall problem, again for black plates. They introduced the concept of passage transmittance, which Tien and Yuen [9] later combined with the exponential kernel approximate method for integral equations to obtain a closed-form expression for the heat transfer, applicable even if the plates are not black. Usiskin and Siegel [10] also used the exponential kernel approximation, in this instance to treat the related problem of a cylinder whose walls are subjected to a constant heat flux.

Although these studies have largely resolved the purely-radiative problem, only a few studies have examined the coupled problem. Tien and Jagannathan [11] categorized the limiting cases relevant to an evacuated cell (with conductive walls) which is so long that the plate emissivities play no role. Many studies [12] have treated an analogous problem of coupled heat transfer across a homogeneous layer of an absorbing–emitting medium, but although Tien and Yuen [9] exploited the analogy for the purely radiative problem, how the analogy can contribute to the present problem remains unclear.

The present paper treats the problem in four ways, each described in a different section. Section 2 reports heat transfer measurements over a range of experimental conditions. Section 3 defines various models and writes down the governing equations. Section 4 presents solutions obtained by numerical methods and, by comparing the results with the measurements, establishes which models give acceptable accuracy. Finally Section 5 solves the equations analytically, subject to certain simplifying assumptions, and compares the results to the numerical results.

2. EXPERIMENT

The ten hexagonal-celled honeycombs used in the experiments were prefabricated in polyester by the

§ The conditions under which the gas is virtually quiescent, or stationary, are treated elsewhere, e.g. see Cane *et al.* [2].

NOMENCLATURE

A	cross-sectional area of individual honeycomb cell (gaseous part only)
$\mathbf{B}$	6×6 matrix with elements given in Table 2
b	constant in exponential fit given by equation (20)
b_{ij}	elements of matrix $\mathbf{B}$, given in Table 2
c	constant in exponential fit given by equation (20)
D	equivalent circular diameter of honeycomb cell, $\sqrt{(4A/\pi)}$
$\mathbf{E}$	column vector with elements given in Table 2
e_j	elements of vector $\mathbf{E}$, given in Table 2
$F^{n,m}_{i-j}$, $\mathrm{d}F^{n,m}_{i-j}$	specular form factor between surfaces i and j: possible values of i and j are w for elemental ring at z (Fig. 3), w' for elemental ring at z', c for cold plate, and h for hot plate. Superscipts n and m indicate model for wall and hot plate reflection (see listing for n and m)
H	overall depth of honeycomb panel (see Fig. 1)
h_t	overall heat transfer coefficient across honeycomb panel
J_c, J_h	radiosity on cold and hot plate, respectively
$J_w(z)$	local radiosity on wall
$k(r)$	local thermal conductivity: $k(r) = k_g$ for $0 < r < R$; $k(r) = k_s$ for $R < r < R+t$
k_e	see equation (15)
k_g, k_s	thermal conductivity of gas and wall material, respectively
L	height of honeycomb panel (see Fig. 1)
m	index indicating whether the hot plate is being treated as a diffuse or specular reflector: $m = 1$ for diffuse, $m = 2$ for specular
n	index indicating whether apparent cell wall is being treated as a specular or diffuse reflector: $n = 1$ for diffuse; $n = 2$ for specular
P	see equation (28)
$q_{cw}(z)$	local conductive flux out of wall at coordinate z
$q_{rw}(z)$	local radiant heat flux delivered to wall at coordinate z
R	$D/2$
r	radial coordinate (see Fig. 3)
$\bar{T}(z)$	see equation (14)
$T(r, z)$	local temperature at coordinates r, z
T_c, T_h	respective temperatures of cold and hot plates bounding honeycomb panel
$T_w(z)$	local wall temperature at location z
t	width of annulus (Fig. 3) having same area as cross-sectional area of one cell's demi-wall
t_h	width of wall between individual cells (see Fig. 1).
W	see equation (26)
W_p	overall width of honeycomb panel (see Fig. 1)
w	width of individual hexagonal honeycomb cell (see Fig. 1)
Y_c, Y_h	$T_c^4/(T_h^4 - T_c^4)$ and $T_h^4/(T_h^4 - T_c^4)$, respectively
z, z'	coordinates (see Fig. 3).

Greek symbols

α	$1-\tau-\rho$
β_c, β_h	$J_c/\sigma(T_h^4 - T_c^4)$ and $J_h/\sigma(T_h^4 - T_c^4)$, respectively
$\gamma_1 \ldots \gamma_4$	constants in general solution for ψ, equation (29)
γ_5, γ_6	$\gamma_5 = \beta_h$; $\gamma_6 = \beta_c$
γ	column vector whose transpose is $(\gamma_1, \gamma_2 \ldots \gamma_6)$
δ_{ij}	Kronecker delta
ε	total emissivity of cell wall
$\varepsilon_c, \varepsilon_h$	respective emissivities of cold and hot plates bounding honeycomb panel
η	z/D
λ	$1 - e^{-2b\mu}$
μ	$L/2D$
ν_1	$b^{-1} + \mu$
ν_2	$b^{-1} - \mu$
ξ	z'/D
ρ	total reflectance of cell wall to black-body radiation at T_h or T_c
σ	Stefan–Boltzmann constant
τ	total transmittance of cell wall to black-body radiation at T_h or T_c
τ_n	total biangular transmittance of cell wall for radiation incident in the normal direction and transmitted in the normal direction
$\tau_{\lambda n}$	spectral biangular transmittance of cell wall for radiation incident in the normal direction and transmitted in the normal direction
ϕ_1, ϕ_2, ϕ_3	$\phi_1 = e^{P\mu}$, $\phi_2 = \phi_1^{-1}$, $\phi_3 = \phi_1 - \phi_2$
Ω_1	$(1-\varepsilon_h)/c$
Ω_2	$(1-\varepsilon_c)/c$
ω	$b(1-(1-\varepsilon)P^2/W)^{2-n}$
ω_1	$\omega(P+b)^{-1}$
ω_2	$\omega(P-b)^{-1}$.

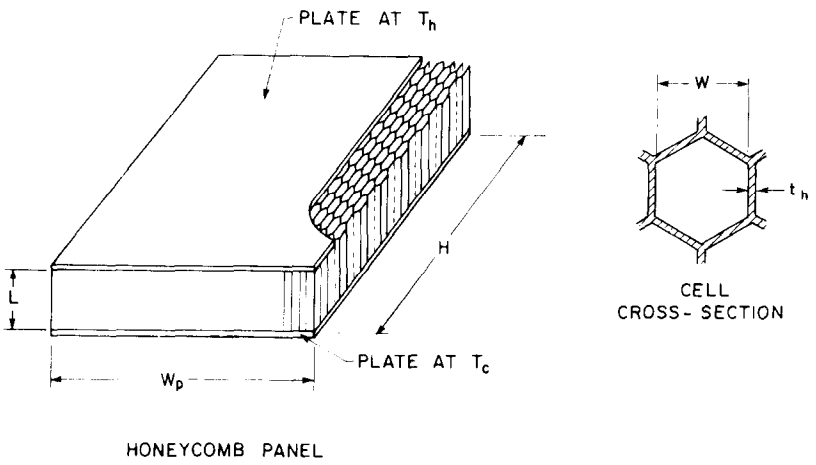

FIG. 1. Sketch of a honeycomb (left) and an individual honeycomb cell (right) showing relevant dimensions. Each cell is a regular hexagon in cross-section.

Hexcel Company of Dublin, California. They came in various dimensions. Seven had cell width w nominally equal to 10 mm and three had w nominally equal to 13 mm. The lengths L ranged in steps from 25 to 100 mm, and the average wall thickness t_h was constant at 0.082 ± 0.002 mm. For each honeycomb the outside dimensions of the entire panel were $W_p = 510$ mm and $H = 560$ mm. The gas inside the cells was air for all tests.

An apparatus used previously for natural convection studies [2] provided the means for measuring the overall heat coefficient h_t across each honeycomb. The plane layer between its two 10 mm thick constant-temperature copper plates contained the honeycomb under test. For the present experiments the plate temperatures were set at $T_h = 306$ K for the hot plate and $T_c = 298$ K for the cold plate. The apparatus measures h_t by a refined version of the guarded heater plate method. The power to an electrically heated 'heater-plate' (125 by 125 by 3 mm thick and fitted into a recess in the hot plate) is adjusted until the temperature difference between it and the hot plate—as sensed by a heat flux meter sandwiched in the recess—is very nearly zero. The measured electric power is then corrected for the residual heat flow, which is determined from the e.m.f. output of the heat flux meter. Dividing this corrected power by the heater plate area and $(T_h - T_c)$ gave h_t within an experimental error* of $\pm(0.01\ \mathrm{W\ m^{-2}\ K^{-1}} + 1\%)$.

The surface finishes of the two plates significantly influence h_t; indeed, by dictating the values for the plate emissivities ε_h and ε_c, they constituted part of the subject under test. Tests incorporated two different surface finishes: painting with black paint, which produced an emissivity of 0.88 ± 0.01, and cleaning and polishing, which produced the emissivity of polished copper, or 0.065 ± 0.01. (Both of these room temperature emissivities were measured using a Gier–Dunkle Model DB-100 Infrared Reflectometer.) The two surface finishes were applied to the plates to give three different combinations of emissivities: $\varepsilon_h = 0.88$ and $\varepsilon_c = 0.88$ (the paint–paint combination); $\varepsilon_h = 0.065$ and $\varepsilon_c = 0.88$ (the polished–paint combination); and $\varepsilon_h = 0.065$ and $\varepsilon_c = 0.065$ (the polished–polished combination). Ten honeycombs and three surface finish combinations yielded 30 different possible experiments in which h_t could be measured, and all but two of these experiments were completed.

Tests were conducted with the plates and honeycomb in a pressure vessel, where the pressure was maintained at about 10mm Hg, and with the plates oriented in their horizontal position with the heated plate below (unstable configuration). This pressure level was selected to eliminate free convection within the panel, while avoiding rarefaction effects. The absence of these effects was confirmed by noting that the heat transfer did not change significantly when the pressure was increased in small steps, nor when the plates were rotated until the hot plate was above.

Measuring the cell dimensions formed part of the experimental procedure. With the test honeycomb placed centrally on the 560 by 610 mm hot plate, the number of cells over the heater plate was counted. Dividing the heater plate area by the result and subtracting the calculated cross-sectional area of one cell's wall gave the internal cross-sectional area A of one cell. For convenience this result was re-expressed in terms of an equivalent circular diameter $D = \sqrt{(4A/\pi)}$. Measurements on each honeycomb of a given nominal cell width gave the same value of D to within its experimental uncertainty (± 0.2 mm), so a single value was used for all such honeycombs. Because of variations (0.1 mm) in the honeycomb height, an exact

* The chief components in this error were a 0.06 K uncertainty in $(T_h - T_c)$, and a 0.05 mV uncertainty in the e.m.f. output of the heat flux meter, whose sensitivity was about $2\ \mathrm{W\ m^{-2}\ mV^{-1}}$.

fit on each plate face was not achieved when the cold plate was lowered onto the honeycomb. The plate spacing L, measured at eight locations at the outer edge and averaged, had an experimental uncertainty of ± 0.1 mm.

The radiant properties of the honeycomb's polyester cell walls were measured twice: once for the total normal-hemispherical values and once for the spectral bi-angular values. The Gier–Dunkle DB-100 Reflectometer measured the total normal-hemispherical values of the transmittance τ, the reflectance ρ, and the absorptance α. Ordinarily one uses this instrument to measure the radiant properties of an *opaque* sample, but by taking two measurements on a diathermanous sample—each with a different opaque surface of known reflectivity behind it—one can determine the radiant properties of a thin *diathermanous* sample as well [13]. (See Appendix for details.) This technique yielded the values $\rho = 0.12 \pm 0.02$, $\alpha = 0.43 \pm 0.02$, and $\tau = 0.45 \pm 0.02$. Since the black-body source in this instrument is at (nearly) the same temperature as the sample, the wall emittance ε is equal to its absorptance, so $\varepsilon = 0.43 \pm 0.02$. A spectrophotometer was used to measure the spectral bi-angular normal–normal transmittance $\tau_{\lambda n}$ over the relevant wavelength range from 2.5 to 50 μm. It revealed windows at the short wavelengths (e.g. from 2.5. to 2.7 μm and from 3.6 to 4.5 μm), in which $\tau_{\lambda n}$ was nearly constant at 0.7, and many closely-spaced absorption bands at the longer wavelengths. These results suggested only modest radiant scattering by the wall. A comparison of the wall's bi-angular normal–normal total transmittance τ_n (computed by convoluting this $\tau_{\lambda n}$ curve with the room temperature black-body spectrum) with the normal-hemispheric total value supported this suggestion. It gave $\tau_n = 0.39 \pm 0.02$ compared to $\tau = 0.45 \pm 0.02$, indicating that the wall scattered only about 6% of incident radiation.

Table 1 tabulates the results of the D, L, and h_t measurements, and Fig. 2 plots h_t vs L/D. Qualitatively the plots show trends expected from the DMA. Quantitatively, however, the agreement of the data with the DMA is unsatisfactory, as will be shown in Section 4.

3. MODELS AND GOVERNING EQUATIONS

As one moves in either direction along the normal to a cell wall, starting at the wall's mid-plane, identical conditions are encountered. This symmetry permits certain simplifications. Clearly each such mid-plane represents an adiabatic surface to its adjacent cells. It also represents a perfect (100%, specular) mirror, since for every ray leaving a cell by transmission through the wall, another ray penetrates from an adjacent cell travelling along the line into which the perfect mirror would have reflected the original leaving ray. To the rest of the cell, the perfect mirror and its thin adjacent demi-wall appear like an opaque wall, whose reflectivity ρ_e is equal to the sum of the reflectance ρ and transmittance τ of the actual wall and whose effective emissivity ε_e is therefore equal to the emittance ε of the actual wall. Thus one need only consider a single isolated cell with opaque and adiabatic walls of thickness equal to one-half the actual wall thickness.

Should these apparent opaque walls be modeled as diffuse or specular? If the actual wall has rough faces and is internally heterogeneous, scattering will be strong and the diffuse model is preferable, even though the perfect mirror is specular. Smooth faces and homogeneous materials would clearly dictate the specular model. Since scattering is greatest at shorter wavelengths, a wall which appears clear in the visible region is also likely to be clear (non-scattering) in the more relevant 3–30 μm wavelength region. A comparison—like that outlined in Section 2—of the hemispheric-normal transmittance of the actual wall with its biangular normal–normal value will also indicate the relative importance of scattering. The theory outlined below is flexible: it embraces apparent walls which are either perfectly diffuse (denoted by an index $n = 1$) or perfectly specular ($n = 2$). Because they showed little scattering, the polyester walls of the experiments were expected to follow the specular model more closely.

The theory is also flexible in its choice of model for the hot plate reflectance, which could be modeled as diffuse (denoted by $m = 1$) or specular ($m = 2$). The black paint finish of the experiments should follow the diffuse

Table 1. Measured total heat transfer coefficients across honeycomb panels

Honeycomb designation number	D (mm)	L (mm)	$\frac{L}{D}$	h_t, (W m^{-2} K^{-1}) $\varepsilon_h = 0.88$, $\varepsilon_c = 0.88$	$\varepsilon_h = 0.065$, $\varepsilon_c = 0.88$	$\varepsilon_h = 0.065$, $\varepsilon_c = 0.065$
1	10.6	25.4	2.40	4.27	2.78	2.26
2	10.6	33.8	3.19	3.70	2.33	1.95
3	10.6	43.3	4.08	3.22	2.09	1.74
4	10.6	50.4	4.75	3.04	1.95	1.61
5	10.6	63.3	5.97	2.63	1.79	1.49
6	10.6	76.0	7.17	2.37	1.66	1.37
7	10.6	101.9	9.61	1.96	1.43	1.17
8	14.1	33.7	2.39	4.25	—	—
9	14.1	66.6	4.72	3.05	1.86	1.46
10	14.1	100.7	7.14	2.41	1.60	1.27

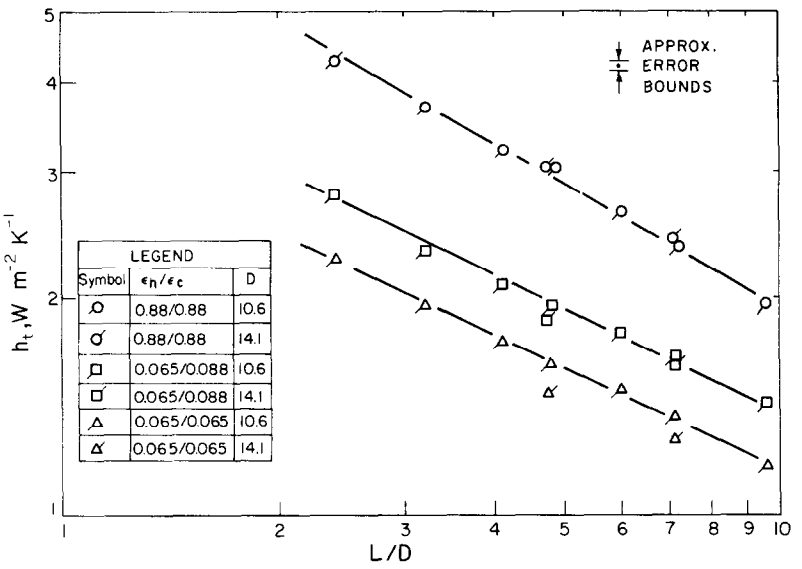

FIG. 2. Plot of measured heat transfer coefficient h_t against L/D for various cell diameters D and combination of plate emissivities ε_h and ε_c.

model, and the polished copper finish should follow the specular model. For reasons of simplicity, the cold plate was uniformly modeled as diffuse, and all surfaces were modeled as grey.

The isolated hexagonal cell was approximated by two concentric circular cylinders (Fig. 3(a)) with a gaseous inner cylinder and a thin solid annular space (not shown as thin in the figure). The radius R of the inner cylinder was made one half the equivalent circular diameter D, thereby matching the inner cylinder's cross-sectional area to that of the inner hexagon. (Provided the cross-sectional areas of circular and hexagonal cylinders are matched, the diffuse end-to-end view factors were found to be virtually the same for the two shapes.) The thickness t was chosen so that the cross-sectional area of the annular space matched the cross-sectional area of the hexagonal demi-wall of thickness $t_h/2$.

Since the walls are thin (in the experiments, t was less than $D/100$) and since a solid plastic's thermal conductivity k_s exceeds by an order of magnitude a gaseous conductivity k_g (in the experiments $k_s = 0.33$ W

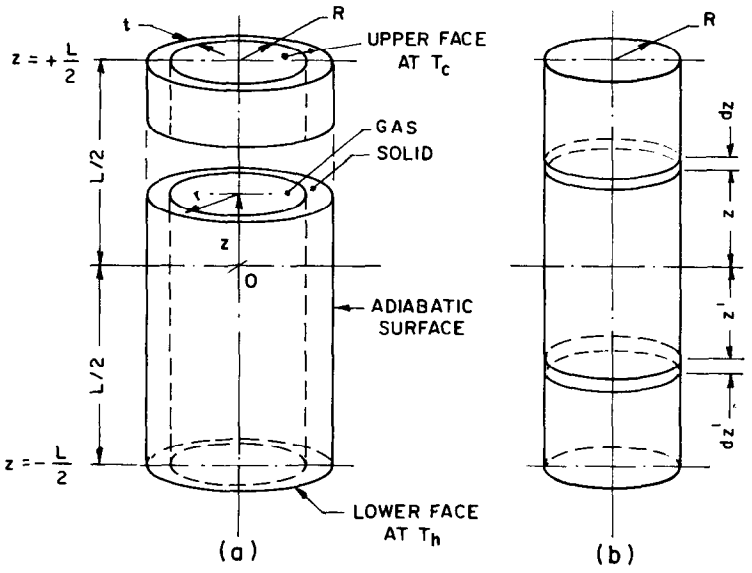

FIG. 3. Sketch showing relevant dimensions and coordinate systems for the cylindrical cells modeling the hexagonal cells. (a) Shows the total cell, including the wall of thickness t. (b) Shows only the gaseous part of the cell.

$m^{-1}K^{-1}$ and $k_g = 0.026\ W\,m^{-1}K^{-1}$), the temperature should vary little in the radial direction across the wall thickness. Thus the absorption and emission, as well as the reflection, of radiation by the apparent wall can be assumed to occur at the (gas–solid) interface rather than inside the wall itself.

3.1. *Governing equations*

An economy in writing the governing equations is achieved by using the approximation that the radiosity is uniform over each of the plates. Solutions of the more general equations for specific cases showed that this approximation does not introduce significant (>1%) errors. Hence the equations written below incorporate this approximation.

Using the coordinate system in Fig. 3, the equations governing the diffuse radiosities $J_w(z)$, J_h, and J_c on the walls, hot plate, and cold plate are

$$J_w(z) = \varepsilon\sigma T_w^4(z) + (1-\varepsilon)\left\{J_h F^{n,m}_{w-h}(z) + J_c F^{n,m}_{w-c}(z) + \int_{-L/2}^{L/2} J_w(z)\frac{dF^{n,m}_{w-w'}(z',z)}{dz'}dz'\right\}\delta_{n1} \quad (1)$$

$$J_h = \varepsilon_h\sigma T_h^4 + (1-\varepsilon_h)\left\{J_c F^{n,m}_{h-c} + \int_{-L/2}^{L/2} J_w(z')\frac{dF^{n,m}_{h-w'}(z')}{dz'}dz'\right\}\delta_{m1} \quad (2)$$

and

$$J_c = \varepsilon_c\sigma T_c^4 + (1-\varepsilon_c)\left\{J_c F^{n,m}_{c-c} + J_h F^{n,m}_{c-h} + \int_{-L/2}^{L/2} J_w(z')\frac{dF^{n,m}_{c-w'}(z')}{dz'}dz'\right\} \quad (3)$$

where δ_{ij} is the Kronecker delta, $F^{n,m}_{i-j}$ denotes a (specular) view factor, and superscripts n and m indicate the model for the reflection on the walls and on the hot plate. Expressions for $dF^{1,1}_{w-w'}(z',z)$ and $dF^{2,1}_{w-w'}(z',z)$ have been reported previously [14] and will not be repreated here. All other relevant view factors can be deduced from these expressions using standard flux algebra; equations (21) and (22) below give some of the details, and the rest are given elsewhere [15].

The equation governing the local temperature $T(r,z)$ in both the solid and the gas

$$\frac{1}{r}\frac{\partial}{\partial r}\left(r\frac{\partial T}{\partial r}\right) + \frac{\partial^2 T}{\partial z^2} = 0 \quad (4)$$

is subject to the boundary conditions

$$\frac{\partial T}{\partial r} = 0 \quad \text{at} \quad r = 0,\ r = R+t \quad (5)$$

$$T = T_h, T_c \quad \text{at} \quad z = -L/2, L/2. \quad (6)$$

In addition, at the interface $r = R$ the radiant and conductive fields must agree, so that

$$T(R,z) = T_w(z) \quad (7a)$$

and

$$q_{rw}(z) = q_{cw}(z) \quad (7b)$$

where $q_{rw}(z)$, the local radiant heat flux into the interface, is given by

$$q_{rw}(z) = \varepsilon\left(\sigma T_w^4(z) - J_h F^{n,m}_{w-h}(z) - J_c F^{n,m}_{w-h}(z) - \int_{-L/2}^{L/2} J_w(z')\frac{dF^{n,m}_{w-w'}(z,z')}{dz'}dz'\right) \quad (8)$$

and $q_{cw}(z)$, the local net conductive heat flux out of the interface, is given by

$$q_{cw}(z) = \left(k(r)\frac{\partial T}{\partial r}\right)_{r=R^+} - \left(k(r)\frac{\partial T}{\partial r}\right)_{r=R^-} \quad (9)$$

in which $k(r)$ denotes the local thermal conductivity.

Once equations (1)–(9) have been solved for $T(r,z)$, $T_w(z)$, $J_w(z)$, $J_w(z)$, J_c, and J_h, one can find h_t from

$$h_t = \left(q_c + q_r\frac{R^2}{(R+t)^2}\right)\Big/(T_h - T_c) \quad (10)$$

where q_c, the heat flux conducted out of the hot plate, is given by

$$q_c = \left\{\int_0^{R+t} k(r)\left(-\frac{\partial T}{\partial z}\right)_{z=-L/2} 2\pi r\ dr\right\}\Big/(\pi(R+t)^2) \quad (11)$$

and q_r, the heat flux radiated out of the inner part of the hot plate, is given by

$$q_r = \varepsilon_h\left(\sigma T_h^4 - J_c F^{n,m}_{h-c} - \int_{-L/2}^{L/2} J_w(z')\frac{dF^{n,m}_{h-w'}(z')}{dz'}dz'\right). \quad (12)$$

3.2. *The 1-D model*

Intuition suggested that the temperature variations in the radial direction may be very much less than $(T_h - T_c)$. Thus a model (the 1-D model) that ignores these temperature variations may simplify the problem without loss in accuracy. Multiplying equation (4), first by the local conductivity $k(r)$ and then by the local area $2\pi r\ dr$, and then integrating the result from 0 to $R+t$ yields expressions for the two gradients in equation (9). These two expressions may be substituted into equation (9), and the result into equation (7b), to yield

$$q_{r,w} = \frac{k_e(R+t)^2}{2R}\frac{d^2\bar{T}(z)}{dz^2} \quad (13)$$

where $\bar{T}(z)$, the weighted mean temperature at any z, is given by

$$\bar{T}(z) = \int_0^{R+t} k(r)T(r,z)2\pi r\ dr \Big/ \int_0^{R+t} k(r)2\pi r\ dr \quad (14)$$

and where k_e, an area-weighted average thermal conductivity, is given by

$$k_e = \frac{\pi R^2 k_g + (\pi(R+t)^2 - \pi R^2)k_s}{\pi(R+t)^2}. \quad (15)$$

The fundamental assumption of the 1-D model is that $T(R, z) = \bar{T}(z)$, so that (from equation (7a))

$$T_w(z) = \bar{T}(z). \tag{16}$$

Combining equation (8), (13), and (16) gives

$$\frac{k_e(R+t)^2}{2R}\frac{d^2T_w(z)}{dz^2} = \varepsilon\left(\sigma T_w^4(z) - J_h F^{n,m}_{w-h}(z) - J_c F^{n,m}_{w-h}(z) - \int_{-L/2}^{L/2} J_w(z')\frac{dF^{n,m}_{w-w}(z,z')}{dz'}dz'\right). \tag{17}$$

Equation (11) simplifies to

$$q_c = -k_e\left(\frac{dT_w(z)}{dz}\right)_{z=-L/2} \tag{18}$$

Equations (1)–(3), and (17)—the four governing equations of the 1-D model—must satisfy boundary conditions $T_w(L/2) = T_h$ and $T_w(L/2) = T_c$. Solutions to these equations are substituted into equations (10), (12), and (18) to find h_t.

4. NUMERICAL SOLUTION

An iterative method of solving the 1-D model equations was used. Nodes (called wall nodes) were first established at points along the wall consistent with Gaussian quadrature. Using an initial guess for the J_w-distribution, equations (2) and (3) were solved simultaneously for J_c and J_h using Gaussian quadrature for the integrals. Next equation (17) was solved numerically for the values of T_w at the wall nodes, and a new J_w-distribution was determined from equation (1). This completed one iteration cycle, cycles being repeated to convergence. The numerical analogs of equations (10), (12), and (18) then yielded h_t.

The method for the full equations (called the 2-D model) followed similar steps, but the numerical solution of equation (17) was replaced by the numerical solution of the steady diffusion equation (equation (4)). Surfaces of constant r or z divided the inner cylinder into elemental volumes, each with a central node (called an interior node). An energy balance on each volume gave a set of algebraic equations for the nodal temperature, constituting the finite-difference analog of equation (4). Equations (5) and (6) and the finite-difference analogs of equations (7)–(9) provided the boundary conditions. Once J_h, J_c, and $J_w(z)$ had been specified, a tri-diagonal matrix solver determined the nodal temperature—including those of the wall nodes.

Grid refinement studies showed that 32 wall nodes gave acceptable accuracy, so subsequent computational runs used this number. The required test runs for the 1-D model with $L/D = 10$ showed that using 10, 20, and 32 wall nodes produced differences in h_t of 3, 1 and 0.2% from the infinite-node asymptote. Smaller values of L/D reduced these differences. Runs for the 2-D model used 20 interior nodes for each of the 32 wall nodes.

The numerical algorithms were checked in several special cases by comparing their predictions with independently-obtained results. Runs with $m = 1$ (diffuse walls), black plates, and $k_e = 0$ reproduced the Hottel–Keller results to within 1% of h_t. The second check compared against an analytical solution. As explained in Section 5, in the limiting case $T_h/T_c \to 1$ the 1-D problem yields an analytical solution if $m = 1$ and—with appropriate revisions to the other view factors—the view factor derivative $dF^{n,m}_{w-w}(z', z)/dz'$ is replaced by $c_1 \exp(-b_1|z-z'|)$ where c_1 and b_1 are constants. Making these changes to the numerical equations produced computed values of h_t within 1% of those from the analytical solution. Except for the ratio T_h/T_c, the values of the various parameters (D, L, ε, k_s, k_g, etc.) chosen for this check were the same as the values they took on in the experiments—that is, the computational runs simulated the experiments.

Solutions to the 1- and 2-D model equations were compared and found to be in close agreement. The necessary computational runs simulated six of the 28 experiments, and the two solutions agreed to within 0.3%, which was within the 0.5% error inherent in the 2-D solution algorithm. It was concluded that the 1-D model gives a sufficiently accurate solution to the problem, and it was therefore adopted for each of the set of computational runs which followed.

The first set of runs simulated the experiments having the painted–painted combination of plate finishes, and their computed values of h_t are compared with the measured values in Fig. 4. The set included runs with $n = 1$ (diffuse walls) and runs with $n = 2$ (specular walls). The runs plotted in the figure assumed $m = 1$ (diffuse hot plate), but runs with $m = 2$ (specular hot plate) gave essentially the same values of h_t. These results confirm that the specular model is the more correct representation of the apparent opaque wall corresponding to the experimental polyester honeycombs. The numerical predictions using this model agree with

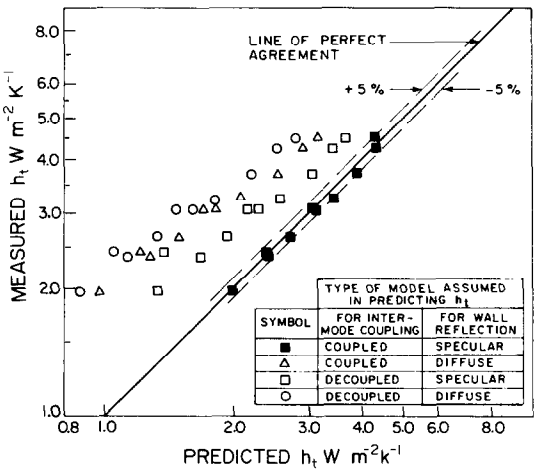

FIG. 4. Comparison of the measured h_t with the h_t computed by solving the governing equations by numerical methods, using various models for the intermode coupling and the wall reflection. This comparison is for the painted–painted ($\varepsilon_h = \varepsilon_c = 0.88$) combination of plate emissivities.

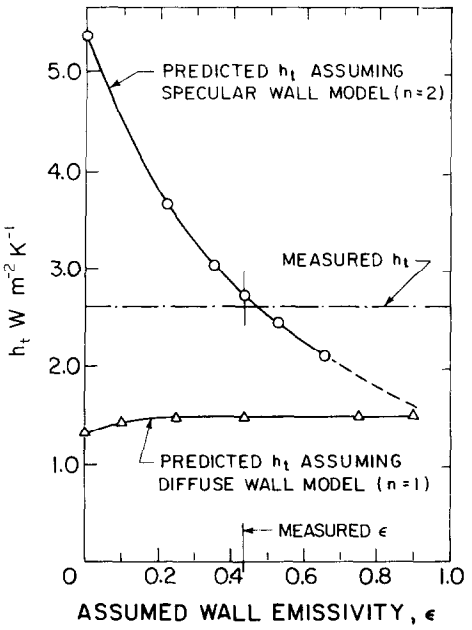

FIG. 5. Sensitivity study indicating the sensitivity of one of the solutions shown in Fig. 5 to the assumed wall emissivity ε.

the measured values with an average deviation of only 3% (the maximum deviation is 7%), whereas the predictions using the diffuse model showed deviations ranging from 50 to 100%. Figure 4 also plots the values of h_t computed using the DMA; they are seen to substantially underpredict the measured values regardless of which wall model is used.*

A sensitivity study, the results of which are plotted in Fig. 5, revealed that the wall emissivity ε affects h_t substantially. Carried out for honeycomb number 5, the study showed that only by using a wall emissivity ε of 0.45 ± 0.02 can the numerical analysis predict the experimental value of h_t to within 4%. (The measured value of ε was $0.43(5) \pm 0.02$.) Thus at least part of the difference between the computed and measured values of h_t can be attributed to the error in measuring ε. Other experimental errors, as well as the assumption that the walls are perfectly grey and specular probably accounts for the remaining difference. For completeness, Fig. 5 also shows the sensitivity to ε for the diffuse wall model; in this instance h_t is relatively insensitive to ε, and agreement with the experimental h_t is not possible for any value of ε.

The second set of runs simulated the experiments having the polished–paint combination of plate finishes, and Fig. 6 shows the results. All the plotted results for this case assume the specular wall model, but results for both specular ($m = 1$) and diffuse ($m = 2$) hot plate models are shown. The numerical results assuming the polished hot plate reflects diffusely ($m = 1$) gives differences of the order of 20%. Only the specular hot plate and the specular wall model gives reasonable agreement: the maximum difference is 11% and the average difference is 6%. The DMA predictions, also plotted in the figure, underpredict the measured h_t by amounts even greater than they do in the paint–paint combination.

The third set of runs simulated the experiments having the polished–polished combination of plate finishes. The polished–paint combination runs had indicated that for best results a polished copper plate should be modeled as specular, so close agreement with the experimental results was not expected in this case (the theory allowed only one plate to be specular). This notwithstanding, the coupled theory using the specular wall, specular hot plate, and diffuse cold plate models computed values of h_t in reasonable agreement with measurements—in fact the average difference (7%) was only slightly greater than that for the polished–paint combination, and the maximum difference (9%) was less than for the polished–paint combination. The theory uniformly over-predicted the experimental results.

The reason for the failure of the DMA can be understood by referring to the computed temperature profiles on the wall, $T_w(z)$, sketched in Fig. 7. To discuss it we (momentarily) assume the 1-D model, so that $\bar{T}(z) = T_w(z)$. Figure 7 sketches the profiles predicted by the coupled mode theory and the DMA. By its nature the DMA requires two plots: one for the purely conductive solution and one for the purely radiative solution. The radiative solution shows a temperature jump at the plates ($z = \pm L/2$), the magnitude of the jump increasing as the adjacent plate's emissivity is lowered. At any z the difference in the temperatures of the radiant and conductive solutions of the DMA measures the

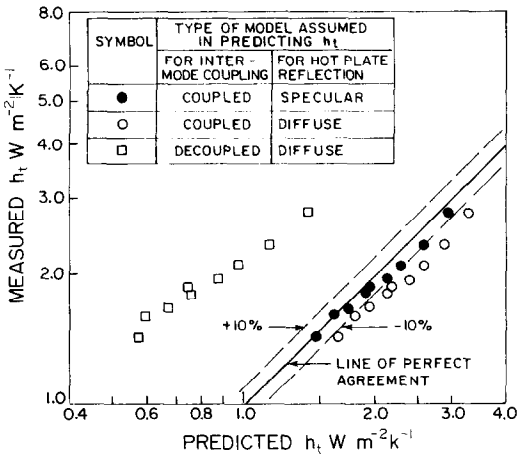

FIG. 6. Comparison of the measured h_t with the h_t computed by solving the governing equations by numerical methods, using different models for the inter-mode coupling and the hot plate specularity. The comparison is for the painted–polished ($\varepsilon_h = 0.065$, $\varepsilon_c = 0.88$) combination of plate emissivities.

* The error in the DMA predictions will likely be less if $\varepsilon \approx 1$. Thus workers [3, 4] using glass honeycombs and nearly black plates and applying a DMA may not encounter substantial errors.

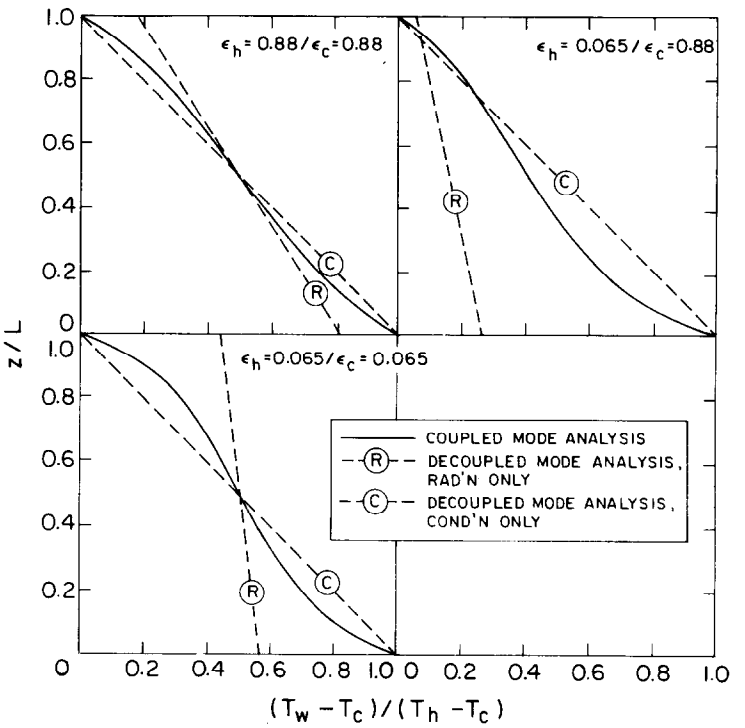

FIG. 7. Plot of the wall temperature profiles (T_w) according to both the decoupled mode and coupled mode analysis.

local potential for inter-mode heat transfer—i.e. for coupling. Near the hot plate, therefore, the heat flows from the conductive mode to the radiative mode, and near the cold plate it flows from the radiative mode to the conductive mode. (A slight difference between $T_w(z)$ and $\bar{T}(z)$ is required to produce this heat flow.) This process produces large temperature gradients at the plates, substantially increasing the conductive heat transfer over that predicted by the DMA. The revised wall profile decreases the radiant transfer from the plate, but not enough to offset the increase in the conductive transfer. The amount of the net increase becomes larger as the radiant solution's temperature jump increases. The limiting case of $\varepsilon_h = \varepsilon_c = 0$ illustrates the point best: there the radiant solution would give zero heat transfer and a flat $T_w(z)$ profile roughly half-way between T_h and T_c; this would produce the maximum temperature jump and the maximum increase of the coupled mode heat transfer over that of the DMA. A very similar coupling occurs in a plane layer of a homogeneous absorbing–emitting gas [12].

In the 2-D case radial conduction is required to permit the conductive mode to feed the radiative mode or vice versa. That the 1-D solution succeeds so well suggests that the radial gradients necessary to drive the condution produce very small temperature differences. Right at the plates the radial gradient must be zero (the plates are isothermal), so the feeding must occur immediately above the plate. This, as well, may explain the success of the 1-D model.

The numerical solution has explored the problem and established which approximations are valid, which invalid. But it has not yielded analytic expressions for h_t and it demands considerable computer time to implement. Thus, as a design tool, it is limited. The more approximate analytical solution which follows provides an easy and inexpensive method of obtaining design information.

5. THE ANALYTICAL SOLUTION

The analysis starts by assuming the 1-D model. It permits the apparent walls to follow either a diffuse or a specular model (i.e. $n = 1$ or 2), but it is limited to perfectly diffuse plates (i.e. $m = 1$ only).

It requires two new approximations. The first, the fourth-power linearization, exploits the fact that $T_h/T_c \approx 1$, so that to a reasonable approximation.

$$\frac{T_w^4 - T_c^4}{T_h^4 - T_c^4} = \frac{T_w - T_c}{T_h - T_c}. \tag{19}$$

The second, the exponential kernel approximation, approximates the view factor derivative $dF_{w-w}^{n,1}(z, z')/dz'$ by an exponential function of $|z-z'|$

$$\frac{dF_{w-w}^{n,1}(z, z')}{dz'} = \left(\frac{c}{D}\right) \exp(-b|z-z'|/D) \tag{20}$$

where c and b are constants. Usiskin and Siegel [10] used this approximation for the diffuse-wall cylinder. We extend its use here to the specular cylinder,

incorporating the constant c (not used by Usiskin and Siegel) in order to better fit the specular view factors.

To fix the values of the c and b in equation (20) we impose two constraints. First equation (20) is forced to satisfy a radiant energy balance on any elemental ring w

$$F^{n,1}_{w-h}+F^{n,1}_{w-c}+\varepsilon^{n-1}\int_{-L/2}^{L/2}\frac{dF^{n,1}_{w-w'}(z,z')}{dz'}\,dz'=1. \tag{21}$$

One can show that

$$F^{n,1}_{w-h}=\varepsilon^{n-1}\int_{-\infty}^{-L/2}\frac{dF^{n,1}_{w-w'}}{dz}\,dz' \tag{22a}$$

and

$$F^{n,1}_{w-c}=\varepsilon^{n-1}\int_{L/2}^{\infty}\frac{dF^{n,1}_{w-w'}}{dz'}\,dz'. \tag{22b}$$

Combining equations (20)–(22), one finds that the first condition is satisfied if

$$b=2c\varepsilon^{n-1}. \tag{23}$$

The second condition is different for $n=1$ and 2. For $n=1$ equation (20) is made to be exact when $z=z'$; this makes $c=1$, and, from equation (23), $b=2$. For $n=2$ the specular view factor $F^{2,1}_{h-c}$, as evaluated using equation (20), is equated to its exact value. This results in

$$\frac{L}{D}\sum_{j=1}^{\infty}\frac{\rho}{j}[(j+L/D)-\sqrt{(j^2+(L/D)^2)}]=\frac{2c}{b^2}\left[b\frac{L}{D}+e^{-bL/D}-1\right]. \tag{24}$$

(The identical relation follows if the specular view factor of the entire wall to itself, as evaluated by equation (20), is equated to its exact value.) Figure 8 plots the results of a simultaneous solution for c of equations (23) and (24) as a function of L/D for various values of ε. To compare the approximate and exact view factor derivatives $dF^{2,1}_{h-c}(z,z')/dz'$, we take the special case $\varepsilon=0.44$ and $L/D=4$, for which $c=1.17$ and $b=1.03$; the inset of Fig. 8 shows the comparison. The fit is not nearly as satisfying as that for the diffuse case, but, as will be seen shortly it ultimately produces reasonable values for h_t.

Incorporating these approximations leads to the analytical solutions for $T_w(z)$. First the approximations—equations (19) and (20)—are substituted into equation (17). A de-dimensionalization uses D for the length scale, $\sigma(T_h^4-T_c^4)$ for the radiant flux scale, and introduces $\psi=(T_w-T_c)/(T_h-T_c)$. This leads to

$$\frac{1}{W}\frac{d^2\psi}{d\xi^2}=Y_c+\psi(\xi)-\beta_h F^{n,1}_{w-h}(\xi)-\beta_c F^{n,1}_{w-c}(\xi)-\varepsilon^{n-1}c\int_{-L/2D}^{L/2D}[Y_c+\psi(\eta)]\exp(-b|\xi-\eta|)\,d\eta \tag{25}$$

in which ξ, Y_c, β_h, and β_c are the dimensionless counterparts of z, σT_c^4, J_h, and J_c, and

$$W=\frac{4\varepsilon\sigma(T_h^4-T_c^4)D}{k_e(T_h-T_c)}. \tag{26}$$

Twice differentiating equation (25) with respect to ξ and removing the resulting integral, by both substituting back into equation (25) and invoking equation (1), gives

$$\psi^{iv}-P^2\psi''=0 \tag{27}$$

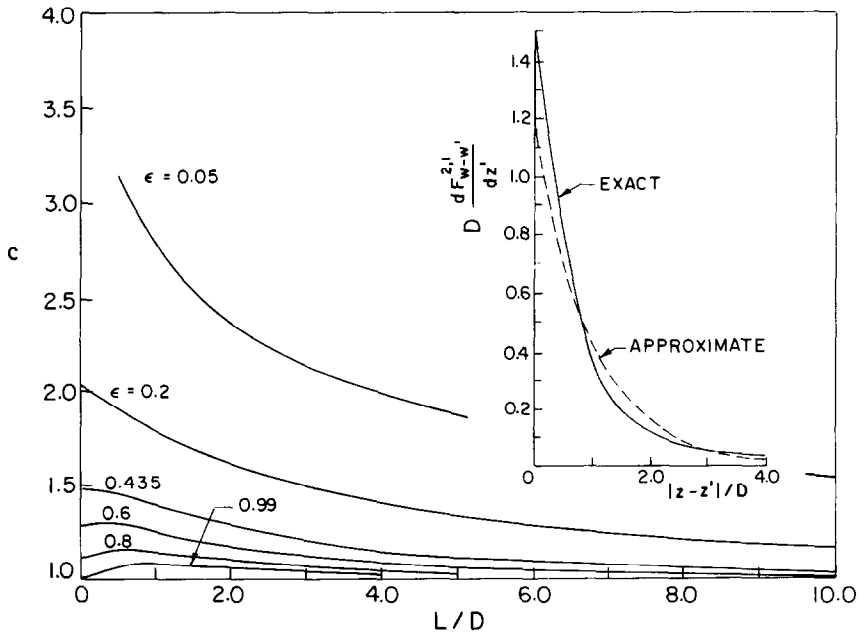

FIG. 8. A plot of the values which c must take in order to make the approximation given by equation (20) satisfy certain integral constraints. The inset shows the goodness of fit obtained when $\varepsilon=0.44$ and $L/D=4$.

Table 2. Table of expressions for elements b_{ij} of matrix **B** and elements e_j of vector **E**

	b_{ij}						e_j
	$j=1$	$j=2$	$j=3$	$j=4$	$j=5$	$j=6$	
$i=1$	1	$-\mu$	ϕ_2	ϕ_1	0	0	1
$i=2$	1	μ	ϕ_1	ϕ_2	0	0	0
$i=3$	-1	$-\nu_1$	$\omega_2\phi_1$	$-\omega_1\phi_2$	0	1	Y_c
$i=4$	-1	ν_1	$-\omega_1\phi_2$	$\omega_2\phi_1$	1	0	Y_c
$i=5$	$\Omega_1\lambda$	$\Omega_1(\nu_1\lambda-2\mu)$	$\Omega_1\omega_2(\phi_3-\phi_1\lambda)$	$\Omega_1\omega_1(\phi_3+\phi_2\lambda)$	-1	$\Omega_1(c-\lambda)$	$-\Omega_1\lambda Y_c-\varepsilon_h Y_h$
$i=6$	$\Omega_2\lambda$	$\Omega_2(2\mu-\nu_1\lambda)$	$\Omega_2\omega_1(\phi_3+\phi_2\lambda)$	$\Omega_2\omega_2(\phi_3-\phi_1\lambda)$	$\Omega_2(c-\lambda)$	-1	$-\Omega_2\lambda Y_c-\varepsilon_c Y_c$

where

$$P=\sqrt{(W+b^2)}. \tag{28}$$

The general solution to equation (27)

$$\psi=\gamma_1+\gamma_2\xi+\gamma_3\,e^{P\xi}+\gamma_4\,e^{-P\xi} \tag{29}$$

must be substituted back into equation (25) to remove spurious roots introduced by the differentiations. Equating like powers of $\exp(\xi)$ in the resulting equation yields two simultaneous linear equations in the constants γ_i. Another such pair is obtained by imposing the boundary conditions $\psi(-L/2D)=1$ and $\psi(L/2D)=0$. The resulting four simultaneous linear equations in the four γ_i can still not be solved, because they contain the unknowns β_h and β_c. For convenience β_h is denoted as γ_5 and β_c as γ_6; two more equations are now required to solve for the new set of six γ_i. The final pair are obtained by substituting equation (29) into equations (2) and (3). They are again found to be linear in the γ_i so the full set of γ_i can now be found by inverting a 6×6 matrix. The full set of six equations can be written

$$\mathbf{B}\gamma=\mathbf{E} \tag{30}$$

in which γ is the column vector whose transpose is $(\gamma_1,\gamma_2,\gamma_3\ldots\gamma_6)$, **B** is the matrix whose elements b_{ij} are given in Table 2, and **E** is a column vector whose elements e_j are given in the same table.

Once γ has been determined, equation (29) for ψ can be substituted into equations (10)–(12) to give h_t. This gives

$$h_t=\frac{k_c}{D}[P\gamma_4\,e^{PL/2D}-\gamma_2-P\gamma_3\,e^{-PL/2D}]$$
$$+\frac{\varepsilon_h}{1-\varepsilon_h}\cdot\frac{\sigma}{(T_h-T_c)}[T_h^4-\gamma_5(T_h^4-T_c^4)]\frac{R^2}{(R+t)^2}. \tag{31}$$

Comparison of the values of h_t calculated from equation (31) with those computed from the numerical solutions of Section 4 gave agreement to within a maximum deviation of 7% for $n=1$ and of 5% for $n=2$. The conditions assumed for this comparison were the same as those appropriate to the experiments (except for the runs assuming the diffuse walls). The analytical predictions generally underpredicted the numerical predictions, and the error increased as the ratio L/D increased.

The analytical solutions are easy to implement and give reasonable accuracy—in fact they often predict the experimental results more closely than the numerical solutions, although this must be coincidental. They are therefore valuable for broad design studies; for example the design plot given in Fig. 9 was produced from the analytical solution. It shows, for instance, that if the plates have high emissivities, a high wall emittance minimizes h_t, whereas if these emissivities are low, a very low wall emittance minimizes h_t. The DMA would have led to very erroneous results in this case.

6. CONCLUSIONS

(1) A coupled-mode analysis based on grey walls predicts measured heat transfer rates within a tolerance of about 5%. The full set of governing equations does not appear to be analytically tractable and must be solved by numerical methods.

(2) Simplifying this coupled-mode analysis by treating the conduction within the gas as 1-D introduces errors of the order of 1% or less.

(3) Further simplifying this coupled-mode analysis,

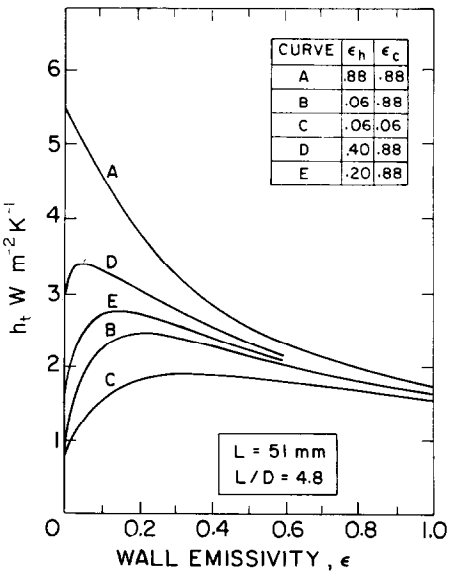

FIG. 9. Plot of h_t vs ε for various conditions, as given by the analytical solution.

by linearizing the fourth-power temperature dependence governing radiant exchange and using the exponential function approximation for the key view factor, permits analytical expressions for the heat transfer to be recovered. Inside the experimental range, these expressions are accurate to within about 10%; they are much easier to implement than the numerical method.

(4) The presence of radiation alters the temperature distribution of the gas from that predicted by a DMA, increasing the wall gradient and thereby raising the heat conducted by the hot plate. Hence a DMA consistently underpredicts the heat transfer.

Acknowledgements—This study was largely financed through a contract with the U.S. Department of Energy under Grant No. EY-76-G-02-2597. This support is gratefully acknowledged. Our thanks also to the National Research Council Canada (Solar Energy Project, Division of Energy) for providing conditions under which one of the authors (K.G.T.H.) could prepare the manuscript. We are also grateful to K. Iynkaran for significant improvements to the analytical solution method.

REFERENCES

1. K. G. T. Hollands, Honeycomb devices in flat plate solar collectors, *Solar Energy* **9**, 159 (1965).
2. R. L. D. Cane, K. G. T. Hollands, G. D. Raithby and T. E. Unny, Free convection heat transfer across inclined honeycomb panels, *Trans. Am. Soc. Mech. Engrs*, Series C, *J. Heat Transfer* **99**(1), 86–91 (1977).
3. H. Buchberg and D. K. Edwards, Design considerations for solar collectors with cylindrical glass honeycombs, *Solar Energy* **18**, 193–203 (1976).
4. J. R. Felland and D. K. Edwards, Solar infrared radiation properties of parallel-plate honeycombs, *J. Energy* **2**(5), 309–317 (1978).
5. K. N. Marshall, R. K. Wedel and K. G. T. Hollands, Economic studies of plastic honeycomb solar collectors, *Proc. Flat Plate Solar Collector Conf.*, Florida State Energy Centre, Cape Canaveral, Florida, Delbert B. Ward, Chairman (1977).
6. D. K. Edwards, *Radiation Heat Transfer Notes*, pp. 137–145, 167–176, 184–186. Hemisphere, Washington (1981).
7. H. C. Hottel and J. D. Keller, Effect of reradiation on heat transfer in furnaces and through openings, *Trans. Am. Soc. Mech. Engrs* **55**, 39–49 (1933).
8. D. K. Edwards and R. D. Tobin, Effect of polarization on radiant heat transfer through long passages, *Trans. Am. Soc. Mech. Engrs*, Series C, *J. Heat Transfer* **89**, 132 138 (1967).
9. C. L. Tien and W. W. Yuen, Radiation characteristics of honeycomb solar collectors, *Int. J. Heat Mass Transfer* **18**, 1409–1413 (1975).
10. C. M. Usiskin and R. Siegel, Thermal radiation from a cylindrical enclosure with specified wall heat flux, *Trans. Am. Soc. Mech. Engrs*, Series C, *J. Heat Transfer* **82**(4), 369–374 (1960).
11. C. L. Tien and P. S. Jagannathan, Analysis of lateral conduction and radiation along two parallel long plates, *AIAA J.* **7**(9), 1806–1808 (1969).
12. E. M. Sparrow and R. D. Cess, *Radiation Heat Transfer* (Augmented edn.), pp. 255–271. Hemisphere, Washington (1978).
13. R. G. Wilkinson, Radiative–conductive heat transfer through a honeycomb panel, M.A.Sc. thesis, Dept. of Mechanical Engineering, University of Waterloo (1979).
14. R. Siegel and J. R. Howell, *Thermal Radiation Heat Transfer* (2nd edn.), pp. 255, 315. Hemisphere, Washington (1981).
15. F. B. Russell, The prediction of stagnant air heat transfer across honeycombs employing numerical methods, M.A.Sc. thesis, Dept. Mechanical Engineering, University of Waterloo (1979).
16. E. A. Christie, Personal communication (1980).

APPENDIX

DETERMINING THE RADIATIVE PROPERTIES OF DIATHERMANOUS FILMS USING THE GIER–DUNKLE DB-100 INFRARED REFLECTOMETER

In the Gier–Dunkle instrument the sample is, for practical purposes, located at the centre of a hemispherical heated cavity, and the total radiation the sample reflects in the normal direction is measured. A relative instrument, it is routinely calibrated against two reference surfaces—one gold, one painted black. Their reflectances, ρ_g for the gold and ρ_b for the black paint, are known from measurements on a separate, absolute instrument.

These reference surfaces provided the two different opaque backing surfaces for the film property measurement. Thus they were placed, one at a time, behind the sample film, to form in each instance a composite surface, and the reflectance of each composite surface was measured, yielding $\rho_{c,g}$ for the gold and $\rho_{c,b}$ for the black paint. An analysis was then required to express the reflectance ρ and transmittance τ of the film in terms of ρ_g, ρ_b, $\rho_{c,g}$, and $\rho_{c,b}$.

The analysis we used modeled the backing surface as perfectly specular and as having reflectance independent of incidence angle. The analysis summed up the contribution, from all possible rays, to the radiation reflected from the composite film in the normal direction, to yield expressions for $\rho_{c,g}$ and $\rho_{c,b}$ in terms of ρ_g, ρ_b, τ, and ρ:

$$\rho_{c,g} = \rho + \frac{\tau^2 \rho_g}{1-\rho\rho_g}; \quad \rho_{c,b} = \rho + \frac{\tau^2 \rho_b}{1-\rho\rho_b}. \tag{A1}$$

Eliminating τ between these two equations gave the required expression for ρ:

$$\rho = \frac{\rho_{c,g}\rho_b - \rho_{b,c}\rho_g}{\rho_b(1+\rho_{c,g}\rho_g) - \rho_g(1+\rho_{c,b}\rho_b)} \tag{A2}$$

and substituting equation (A2) for ρ into either of equations (A1) gave the required expression for τ. Equation (A2) is due to Christie [16], who corrected an error in Wilkinson's equation.

The assumptions of the analysis warrant discussion. The black paint was not specular, but because its reflectance is very low ($\rho_b \approx 0.08$), little error should result from assuming it to be specular (if $\rho_b = 0$, there would be no error). The gold, with $\rho_g \approx 0.98$, was highly specular, but its reflectivity will have an angular dependence. Provided, however, that the film transmits mainly on the beam, little error should follow from neglecting the backing's angular dependence. If ρ_g were equal to unity (which it very nearly is), one could construct mirror images to show that, during a measurement, the sample film and its image are at the centre of a *spherical* heated cavity, where each of their faces is irradiated hemispherically. Since the radiation they reflect or transmit in the normal direction is what is measured, the measurement process should yield a result very close to the normal-hemispherical values of the film's radiative properties.

TRANSFERTS THERMIQUES COUPLES RADIATIFS ET CONDUCTIFS A TRAVERS DES PANNEAUX A NID D'ABEILLE ET A TRAVERS DES CELLULES UNIQUES

Résumé—En l'absence de convection naturelle, la chaleur passe à travers un gaz remplissant un nid d'abeille par conduction et rayonnement. Pour des domaines de collecteur solaire plan, la conduction et le rayonnement sont fortement couplés. Le transfert de chaleur total à travers le panneau est étudié expérimentalement et théoriquement. L'approche expérimentale mesure avec précision le transfert thermique total pour des conditions variées. L'étude théorique propose plusieurs modèles avec leurs équations, et résout les équations par des méthodes numériques ou analytiques. Un modèle basé sur des surfaces grises, avec paroi latérale spéculaire et conduction unidirectionnelle fournit des résultats à 6% près conformes aux mesures.

WÄRMEÜBERTRAGUNG DURCH STRAHLUNG UND LEITUNG AN EINEM HONIGWABEN-PANEL UND AN EINZELNEN ZELLEN

Zusammenfassung—Ohne natürliche Konvektion wird Wärme innerhalb einer gasgefüllten Honigwabe durch Leitung und Strahlung übertragen. In den interessierenden Parameter bereichen bei Kunststoff-Honigwaben von Sonnenflachkollektoren sind Leitung und Strahlung eng miteinander verknüpft. Der Gesamtwärmedurchgang eines Panels wurde experimentell und theoretisch untersucht. Bei den Experimenten wurde der Gesamtwärmedurchgang exakt unter verschiedenen Versuchsbedingungen gemessen. Bei den theoretischen Untersuchungen wurden mehrere Modelle erstellt, ihre Grundgleichungen aufgestellt und durch numerische oder analytische Methoden gelöst. Ein Modell mit einer grauen Oberfläche, spiegelnden Seitenwänden und eindimensionaler Wärmeleitung lieferte Ergebnisse, die um nicht mehr als 6% von den Messungen abweichen.

СОВМЕСТНЫЙ ЛУЧИСТЫЙ И КОНДУКТИВНЫЙ ТЕПЛОПЕРЕНОС ЧЕРЕЗ СОТОВЫЕ ПАНЕЛИ И ЕДИНИЧНЫЕ ЯЧЕЙКИ

Аннотация—В отсутствие естественной конвекции тепло передается через заполненные газом ячейки теплопроводностью и излучением. В исследуемом интервале параметров в пластиковом сотовом слое, находящемся внутри плоской пластины солнечного коллектора, теплопроводность и излучение сильно взаимосвязаны. Суммарный теплоперенос через панель изучался экспериментально и теоретически. В экспериментах проводились высокоточные измерения суммарного теплопереноса при различных условиях. В теоретической части работы предложено несколько моделей, для которых выведены определяющие уравнения, решенные либо численно, либо аналитически. Модель, основанная на предположении серых поверхностей, зеркальных боковых стенок и одномерной теплопроводности, дает результаты, которые с точностью до 6% совпадают с измеренными данными.